# First-Principles Study of One- and Two-Photon Absorption of the H-Bonding Complexes from Monomeric Red Fluorescent Proteins with Large Stokes Shifts

Min-Yi Zhang, Jin-Yun Wang, Chen Sheng Lin, and Wen-Dan Cheng*

State Key Laboratory of Structural Chemistry, Fujian Institute of Research on the Structure of Matter, Chinese Academy of Sciences, Fuzhou, Fujian 350002, China

Ⓢ *Supporting Information*

ABSTRACT: LSSmKate1 and LSSmKate2 are monomeric red fluorescent proteins (RFPs) with large Stokes shifts (LSS). The hydrogen-bonding (H-bonding) network within LSSmKate1 or LSSmKate2, which is composed of a chromophore and some surrounding amino acid residues, supports their special spectral properties. In this work, we propose H-bonding complex models to simulate the H-bonding network of LSSmKate1 and LSSmKate2 and employ the time-dependent density functional theory combining with the sum-overstates method to calculate their one- and two-photon absorption characters. We discuss the influence of the hydrogen bond on the one- and two-photon absorption properties of these H-bonding complexes through intermolecular hyperconjugation of the hydrogen-bond form.
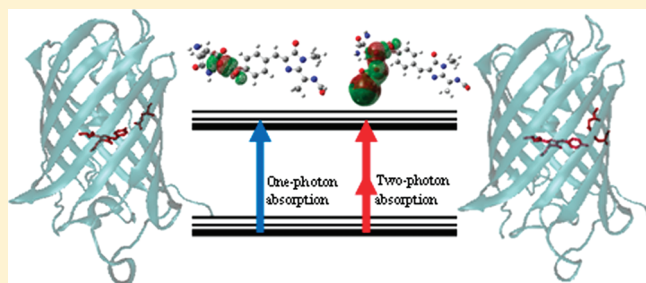
1. INTRODUCTION

Fluorescent proteins (FPs), the great important fluorescent probes, have been widely used in cell biology in molecular labels, noninvasive markers of gene expression, and intracellular protein localization, and so forth.[1,2] Among FPs, red fluorescent proteins (RFPs) are of particular interest because their emission spectrum has a lower signal from cellular autofluorescence, allowing greater imaging depth and less damage to proteins and DNA.[3,4] From the other side, two-photon excitation microscopy (TPEM) has a number of specific advantages, such as less photodamage, enhanced penetration depth, and higher-contrast images in biological samples. It has become a preferred method for live cell and tissue imaging.[5–7] Despite the widespread application of blue-green wavelength range FPs in two-photon microscopy, the use of RFPs is limited by the low power output of Ti-sapphire lasers above 1000 nm currently.[8]

Recently, Piatkevich and co-workers developed two large Stokes shifts (LSS) RFPs from a monomeric far-red FP mKate; named LSS-mKate1 and LSS-mKate2, they exhibit excitation/emission peaks at 463/624 and 460/605 nm, respectively.[9] These two mKate variants with large Stokes shifts allow efficient excitation by standard TPEM sources and would be suitable for multicolor two-photon in vivo imaging when they combine with some blue or green FPs. The far-red FP mKate is substantially brighter than HcRed or mPlum; its chromophore arising from the precursor-yresidue Met63-Tyr64-Gly65 is part of the protein's own poly-peptide and forms the DsRed-like chromophore. LSS-mKate1 and LSS-mKate2 are generated from mKate by substituting some amino acids around the chromophore. The most difference between LSS-mKate1 and LSS-mKate2 is a single amino acid substitution at position 160. According to X-ray structure determination, LSS-mKate1 corresponds to a cis configuration of a neutral DsRed-like chromophore, while LSS-mKate2 corresponds to a trans configuration of a neutral DsRed-like chromophore. Their LSS properties are attributed to the arrangement of some proton acceptor amino acid chains near to chromophore, which build a hydrogen-bonding (H-bonding) network which can support an excited-state proton transfer (ESPT) pathway.[10]

The simple ESPT model has been used to explain the maxima emission peak of green fluorescent protein (GFP) at 508 nm, which corresponds to neutral ground state of GFP chromophore A with absorption peak at 396 nm.[1,11,12] The EPST proton wire of GFP is composed of proton donor chromophore, water25, Ser205, and proton acceptor Glu222. When excited at 396 nm, the proton at excited-state A* rapidly transfer to the Glu222 though the proton wire and form the intermediate excited state denoted I*. The excited state I* is an anionic form that subsequently emits green fluorescence, then decays to ground state I, which converts to the ground state A, completing the wtGFP photocycle.[13,14] Through structure analysis, LSS-mKate1 and LSS-mKate2 have different proton wires. The chromophores hydroxyl and Glu160 compose the H-bonding network in LSSmKate1, and the chromophores hydroxyl, Ser158, and Asp160 compose the H-bonding network in LSSmKate2.[10]
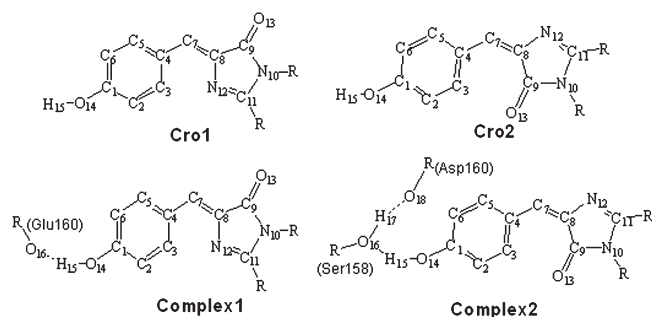
Figure 1. Conformer models: cro1 and cro2 are the isolated chromophores of mKate1 and mKate2, respectively; complex1 and complex2 are the H-bonding complexes of mKate1 and mKate2, respectively.

On the other hand, the formation of H-bonding may lead to the change in the electronic structures and physical chemistry properties of both the proton donor and acceptor.[15,16] Both of the chromophores of LSS-mKate1 and LSS-mKate2 are the proton donor in their H-bonding networks. Undoubtedly, the interacting between the chromophore and amino acid residue via H-bonding would change the electronic structures of chromophore by comparison with that of isolate chromophore. We presume that the H-bonding complex models of chromophore with amino acid residue might provide a better understanding of the physical chemistry properties of LSS-mKate. In past works, many theoretical studies of the physical chemistry properties of FPs usually use the neutral or anionic chromophore models cutting from the H-bonding network.[17−20]

In this paper, we propose the H-bonding complex models which are composed of chromophores and amino acid residues of LSS-mKate1 and LSS-mKate2, respectively, to simulate their H-bonding network. We use these two complex models to study the one- and two-photon absorption properties of LSS-mKate1 and LSS-mKate2. We will discuss the influence of hydrogen bonds on the physical chemical properties of LSS-mKate. To our best knowledge, this is the first theoretical study of LSS-FPs by using a H-bonding complex.

2. COMPUTATIONAL METHODS

2.1. Models. The initial structures of the LSS-mKate1 and LSS-mKate2 were obtained from the Protein Data Bank (PDB IDs: 3NT9 and 3NT3).[9] The isolated chromophores of LSS-mKate1 and LSS-mKate2 are obtained from getting rid of connections to the protein backbone at the appropriate positions, and the dangling bongs are saturated with methyl groups. The H-bonding complex of LSS-mKate1 is composed of glutamic acid residues and chromophores, and the H-bonding complex of LSS-mKate2 is composed of serine, aspartic acid residues, and chromophores; they are also obtained from cutting the connections to the protein backbone at the appropriate positions and the dangling bongs are saturated with methyl group. All of the model structures are presented in Figure 1.

2.2. Theory. Without special indication, all calculations have been performed by the Gaussian 03[21] program package using the density functional theoretical (DFT) method with the B3LYP hybrid functional. Considering the necessity of diffuse functions for full characterization of the hydrogen-bond interaction, we exploit the 6-311++G(d,p) basis set for calculation, which is

considered as the smallest one for H-bonding to obtain reasonable results.[22]

The geometrical structure of each species was optimized by the DFT/B3lyp/6-311++G(d,p) level in the gaseous phase. To evaluate the effect of implicit solvent, we also use the polarizable continuum model (PCM) to optimize the geometrical structure and do other calculations of all of the species.[23,24]

Stabilization energies (ΔE_{stab}) of H-bonding complex have been calculated as follows:

$$\Delta E_{stab} = E_{A*B*}^{opt} - E_{A}^{opt} - E_{B}^{opt} \tag{1}$$

Here, E_{A*B*}, E_A, and E_B are the energy of complex, monomer A, and monomer B, respectively, and the superscript opt denotes that their geometries have been optimized, respectively. The stabilization energy of the H-bonding complex was corrected for basis set superposition error (BSSE) using the method of Boys and Bernardi.[25] The BSSE was corrected by the Boys and Bernardi counterpoise correction scheme as follows:

$$BSSE = E_{A*} + E_{B*} - E_{A*}(A*B*) - E_{B*}(A*B*) \tag{2}$$

where E_{A*} is the energy of the monomer A at the complex geometry with its own basis set and $E_{A*}(A*B*)$ is the energy of the monomer A at the complex geometry with the basis set of complex. For monomer B, the energies of E_{B*} and $E_{B*}(A*B*)$ have the same meaning as E_{A*} and $E_{A*}(A*B*)$, respectively. So the correct stabilization energy of complex is

$$\Delta E_{stab}(corrected) = \Delta E_{stab} + BSSE \tag{3}$$

The TPA efficiency can be characterized by the TPA cross-section $\delta(\omega)$, and the latter can be directly related to the imaginary part of the second hyperpolarizability $\gamma(-\omega;\omega,-\omega,-\omega)$ by[26]

$$\delta(\omega) = \frac{32\pi^4\hbar}{n^2\lambda^2}L^4 \, \text{Im}[\gamma(-\omega;\omega,\omega,-\omega)] \tag{4}$$

where $\gamma(-\omega;\omega,\omega,-\omega)$ is the third-order polarizability, n denotes the refractive index of the medium, and L corresponds to the local-field factor and $L = (n^2 + 2)/3$. Generally, $n = 1.333$ in aqueous and $n = 1.0$ in vacuum. Here, the n value is set to 1.0 in all calculations for systematic comparison.

We calculated $\lim[\gamma(-\omega;\omega,\omega,-\omega)]$ using the sum-overstates (SOS) expression.[27−29] To compare the calculated TPA cross-section value with the experimental value measured in solution, the orientationally averaged (isotropic) value of γ is evaluated, which is defined as:

$$\langle\gamma\rangle = \frac{1}{15}\sum_{i,j}(\gamma_{iijj} + \gamma_{ijij} + \gamma_{ijji}) \quad i,j = x,y,z \tag{5}$$

and when $\langle\gamma\rangle$ is taken into eq 4, the TPA cross section δ is obtained.

Generally, the position and relative strength of the two-photon resonance are to be predicted using the following simplified form of the SOS expression:[30,31]

$$\delta \propto \frac{M_{0k}^2 M_{kn}^2}{(E_{0k} - E_{0n}/2)^2\Gamma} \, \text{(three-state term)}$$

$$+ \frac{M_{0n}^2 \Delta\mu_{0n}^2}{(E_{0n}/2)^2\Gamma} \, \text{(dipole term)} \tag{6}$$

Table 1. Selected Optimized Structural Parameters (Bond Length (Å)) for the Studied Conformers in the Gaseous Phase and in Solvent Water[a]

parameter	cro1		complex1		cro2		complex2	
	gas	water	gas	water	gas	water	gas	water
C1—O14	1.361	1.353	1.315	1.336	1.36	1.351	1.325	1.328
C1—C2	1.401	1.405	1.421	1.412	1.399	1.404	1.415	1.415
C2—C3	1.382	1.382	1.373	1.379	1.385	1.384	1.375	1.374
C3—C4	1.414	1.416	1.423	1.418	1.413	1.415	1.423	1.42
C4—C5	1.409	1.413	1.423	1.416	1.416	1.419	1.423	1.421
C5—C6	1.387	1.385	1.376	1.383	1.382	1.381	1.377	1.382
C1—C6	1.398	1.401	1.417	1.409	1.399	1.403	1.414	1.415
C4—C7	1.443	1.439	1.419	1.434	1.441	1.437	1.422	1.423
C7—C8	1.360	1.366	1.380	1.369	1.368	1.373	1.383	1.382

[a] Gas, B3LYP/6-311++G** ; water, PCM/B3LYP/6-311++G**.

Table 2. Optimized Geometry Parameters (Bond Length (Å) and Angle (Degree)) of H-Bonds of complex1 and complex2 in Gaseous Phase and in Solvent Water[a]

parameter	complex1		complex2	
	gas	water	gas	water
O14—H15	1.047	1.023	1.007	1.01
H15—O16	1.48	1.551	1.616	1.61
O14—O16	2.507	2.559	2.622	2.619
O16—H17			1.004	1.008
H17—O18			1.612	1.61
O16—O18			2.613	2.614
O14—H15—O16 angle	165.37	167.32	178.58	176.45

[a] Gas, B3LYP/6-311++G** ; water, PCM/B3LYP/6-311++G**.

where M_{ij} is the transition dipole moment from the state i to j; E_{ij} is the corresponding excitation energy, the subscripts 0, k, and n refer to the ground state S_0, the intermediate state S_k, and the TPA final state S_n, respectively; Γ is the damping factor of excited state; $\Delta\mu_{0n}$ is the dipole moment difference between S_0 and S_n. in the present work, all damping factors Γ are set to 0.1 eV; this choice of damping factor is found to be reasonable on the basis of the comparison between the theoretically calculated and experimental TPA spectra. The total TPA cross section spectra can be separated into contributions of the dipolar term, which appear only in noncentrosymmetric systems like our investigating model, and the three-state term, which appear in any systems irrespective of symmetry. When only one excited state usually the lowest excited state mainly contributes to all responses, the dipole term become predominant, while, for the higher excited state, the three-state term majorly contributes to the TPA cross section spectra.[32]

Here noted from the SOS formula,[27−29] γ is dependent on the transition dipole moments and the transition energies between state and state; further, the calculations of γ are sensitive to the treatment of electron−electron interactions (EEI) or electron correlation. Generally, to treat the electron correlation by means of configuration interactions in the content of the ab initio or semiempirical HF model, single- and double-excitation configuration interactions (CISD) must be included at least to obtain a correct γ value.[33] However, electron correlation and exchange interactions are included in a natural way in the content of the time-dependent density functional theory (TDDFT) model.[34] Accordingly, it is reasonable that the TDDFT method was employed to perform the excited state and γ calculations.[35,36] However, one should be also warned of the possibility of dangers in computational efforts. Although performing extensive checks of method and basis set dependence is rather limited, the reliability of the computational part is crucial of studies involving the determination of electric hyperpolarizabilities and related properties.[37]

3. RESULTS AND DISCUSSION

3.1. Geometry and Energy. The selected optimized structural parameters for the four conformers (Figure 1) are presented in Table 1. From Table 1, both of the isolate chromophore structures of mKate1 and mKate2 are slightly influenced by using the PCM in

water. Considering the hydrogen-bond interaction with the amino acid residue, from isolate chromophores to H-bonding complexes, the geometry of a chromophore in their H-bonding complexes, especially the phenol ring of chromophore, is variously noteworthy both in the gas phase and in the aqueous phase. For mKate1, we observe that the distances of C1—O14, C2—C3, and C5—C6 shorten, and the distances of C1—C2, C3—C4, C4—C5, and C1—C6 enlarge from isolate chromophore (cro1) to complex (complex1). The shortening of C1—O14 in complex1 indicates the possible pull-force from the oxygen acceptor atom O16. The phenol ring in complex develops to a more quinoidal structure than that in isolate chromophore. For mKate2, the geometry of chromophore has a similar varying trend from isolate chromophore to complex as mKate1 above.

The geometric parameters at a hydrogen-bond site of complex1 and complex2 are presented in Table 2. The distant O14—O16 of complex1 is 2.507 Å in the gaseous phase and 2.559 Å in the aqueous phase. When including the PCM calculation, the dipole—dipole interaction between polar solvent and solute molecules may suffice to lose considerably the intramolecular forces in solution. Thus, the exertion of the polar solvent reaction field leads to the weakening of the hydrogen bond. We observe that the O14—H15 bond is 1.047 Å and the H15—O16 bond is 1.480 Å in the gaseous phase, while the O14—H15 bond shortens by 0.024 Å and H15—O16 bond elongates by 0.071 Å in the aqueous phase. These indicate a strong asymmetric H-bond of complex1 with a chromophore as a proton donor and Glu160 as a proton acceptor. We also find that there are two strong asymmetric H-bonds of O14—O16 and O16—O18 in complex2. However, the influence of aqueous phase is less serious to the two H-bonds of complex2 than the only one H-bond of complex1. The O14—O16 bond is 2.622 Å in the gaseous phase and 2.619 Å in the aqueous phase, while the O16—O18 bond is 2.613 Å in the gaseous phase and 2.614 Å in aqueous phase. By comparing the three H-bond distances, the H-bond O14—O16 of complex1 is stronger than the other two H-bonds of complex2.

The dipole moments for different conformers are summarized in Table 3. The dipole moment of each conformer is found to be larger in aqueous solution than in the gaseous phase. Both of the H-bonding complexes of mKate1 and mKate2 have a larger dipole moment than their isolate chromophores, respectively. The influence of the aqueous phase on the stability of different conformers is also presented in Table 3. The calculated energy of

10752

dx.doi.org/10.1021/jp203977m |J. Phys. Chem. B 2011, 115, 10750–10757

Table 3. Calculated Dipole Moments (μ in Debye) for the Studied Conformers and Calculated Energy (ΔE in kcal/mol) of Each Conformer in the Aqueous Phase Relative to Its Energy in the Gaseous Phase, Respectively[a]

parameter	cro1		complex1		cro2		complex2	
	gas	water	gas	water	gas	water	gas	water
μ	4.49	7.53	10.18	15.18	3.50	5.78	7.29	10.06
ΔE	0	−20.34	0	−57.02	0	−19.44	0	−55.53

[a] Gas, B3LYP/6-311++G** ; water, PCM/B3LYP/6-311++G**.

Table 4. One-Photon Absorption Properties of Studied Conformers Obtained at the TDDFT/B3LYP/6-311++G Level: Oscillator Strengths f, One-Photon Absorption Wavelength λ (nm), and Relevant Excitations**

conformer	λ	f	transition nature	ex λ
cro1	424.7	0.6351	S0→S1, H→L, 0.61112	463[9]
cro1[a]	444.6	0.8249	S0→S1, H→L, 0.62490	
complex1	507.9	0.8096	S0→S2, H→L, 0.59237	
complex1[a]	458.0	0.9365	S0→S1, H→L, 0.62415	
cro2	418.1	0.6937	S0→S1, H→L, 0.60706	460[9]
cro2[a]	431.1	0.9406	S0→S1, H→L, 0.62283	
complex2	465.2	1.0378	S0→S1, H→L, 0.60055	
complex2[a]	460.8	1.0978	S0→S1, H→L, 0.62415	

[a] Using PCM at the B3LYP/6-311++G** level.

each studied conformer in the aqueous phase is relative to its energy in the gaseous phase, respectively. So it is evident to see that the incorporation of a solvent effect (using the PCM in water) has a remarkable influence on the stability of each conformer. The stabilities of both Cro1 and Cro2 are enhanced for about 20 kcal/mol in the aqueous phase. For the H-bonding complex, the influence of the solvent is very noteworthy. The stabilities of both complex1 and complex2 are enhanced for about 55 kcal/mol in the aqueous phase. These mainly are attributed to the effect of the polar solvent water upon the H-bonding complex. We also find that the stability of single chromophore and glutamic acid residues would be enhanced for about 32.72 kcal/mol by forming the O14−H15··· O16 H-bonding complex1. The forming O14−H15···O16 H-bond of complex2 also enhances the stability of complex2 for 22.76 kcal/mol. From these, we find that the O14−H15···O16 H-bond in complex1 is stronger than that in complex2.

3.2. Electronic Structure and One-Photon Absorption Properties. We employ the TDDFT method with 6-311+ +G** basis sets to calculate the one-photon absorption (OPA) properties of the four conformers (Figure 1), shown in Table 4. From this table, we can see that the strongest OPA peaks of all the conformers are corresponding to their first excitation with contributions from the highest occupied molecular orbital (HOMO) to the lowest unoccupied molecular orbital (LUMO), respectively. For isolate chromophores of mKate1 and mKate2, their strongest OPA bands are 425 and 418 nm in the gaseous phase, respectively. When introduction of PCM, the OPA band of mKate1 is red-shifted to 445 nm with a stronger oscillator strength of 0.8249, and the OPA band of mKate2 is red-shifted to 431 nm with a stronger oscillator strength of 0.9406. The OPA calculations of chromophores including implicit solvent effects could result in a better agreement with the experiment.[17] As mentioned above, both mKate1 and mKate2 have two conformations of H-bonding complexes; one is optimized in the gas phase, and the other one is optimized in the aqueous phase. We also include the PCM when calculating the OPA properties of the complexes which are optimized in the aqueous phase. Their OPA properties are presented in Table 4. For mKate1, complex1 calculated in the gaseous phase has the strongest OPA band at 508 nm. Meanwhile, the strongest OPA band of complex1 calculated in aqueous phase is at 458 nm, which is blue-shifted compared with the former and agrees well with the experimental data of 463 nm.[9] For mKate2, complex2 calculated in the gaseous phase has the strongest OPA band at 465 nm. The complex2 calculated in the aqueous phase has the strongest OPA band at 461 nm, which is a little blue-shifted compared with the former and agrees well with the experimental data of 460 nm.[9] When compared with the isolate chromophores of mKate1 and mKate2, the calculated OPA properties of the H-bonding complex, especially

the one which includes the PCM calculation, have better agreements with the experimental ones. It is indicated that the model of the H-bonding complex will approach the actual environment of protein.

Electronic structures are fundamental to interpretation and understanding of the absorption spectra. The calculated frontier orbital energies (HOMO and LUMO) and energy gaps between HOMO and LUMO for all of the conformers are listed in Table 5. The plots of their frontier orbital are shown in Figure 2. The HOMO and LUMO of all of the H-bonding complexes are completely localized on the chromophore and show π and π^* character, respectively. From Table 5, for mKate1 in the gaseous phase, forming the H-bonding complex1 dramatically increases the HOMO/LUMO energies and decreases the energy gaps in general when compared to the isolated chromophore. When considering the solvent effect, the influence of forming H-bonds on the frontier orbital energies is not as serious as in the gaseous phase; however, the HOMO/LUMO energies of H-bonding complex1 also increase, and the energy gaps decrease in general. So the decrease of energy gaps mainly contributes to the red shift OPA band of H-bonding complex1 relative with the isolated chromophore. For mKate2, when compared to the isolated chromophore, the HOMO energy of complex2 increases, and the energy gaps decrease both in the gaseous phase and in the aqueous phase due to the same reason as mKate1. These also result in the red-shift OPA band of complex2. The energy increase of the frontier orbital can be attributed to the increase of the intermolecular charge transfer which was induced by the overlap of molecular orbital of two monomers when forming the H-bonding complex (the intermolecular charge transfer will be discussed in detail in a later section). It is also interesting to see that the H-bonding complex including PCM calculation has blue-shifted the OPA band compared to the complex which is calculated in the gaseous phase. We have known that the exertion of the polar solvent reaction field leads to weakening of the intermolecular hydrogen bond, which would induce the decrease of intermolecular charge transfer and enlarge the HOMO and LUMO gaps. So this finally results in the blue-shift of OPA band in PCM model relative to the gaseous model. In views of the calculations of electronic structures, charge transfers between the molecules lead to the long wavelength OPA peak in H-bonds of complexes.

3.3. Two-Photon Absorption Properties. As mentioned above, the structural model of the H-bonding complex will approach the actual environment of protein for the OPA properties. In this

Table 5. HOMO and LUMO Energies, HOMO-LUMO Energy Gaps (E_{L-H}), and Vertical Excitation Energies (ΔE_{band}) for the Studied Conformers at the B3LYP/6-311++G Level (Energy in eV)**

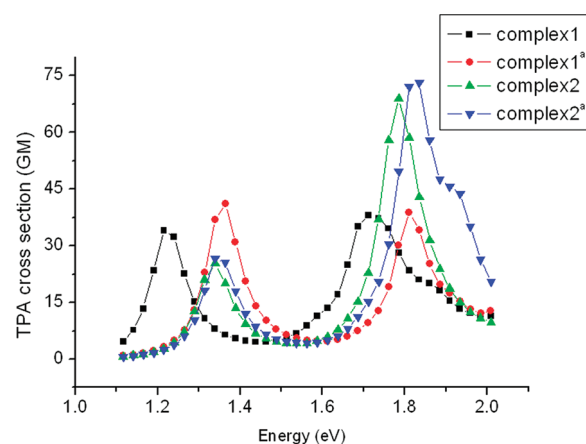|	cro1	cro1[a]	complex1	complex1[a]	cro2	cro2[a]	complex2	complex2[a]
HOMO	−6.04	−6.04	−3.46	−5.86	−6.11	−6.06	−3.80	−5.90
LUMO	−2.95	−3.02	−0.98	−2.91	−3.00	−2.96	−1.10	−3.01
E_{L-H}	3.08	3.02	2.46	2.95	3.11	3.10	2.89	2.89
ΔE_{band}[b]	2.92	2.79	2.44	2.71	2.97	2.88	2.67	2.69

[a] Using PCM at the B3LYP/6-311++G** level. [b] ΔE_{band} is the transition energy to the lowest excitation
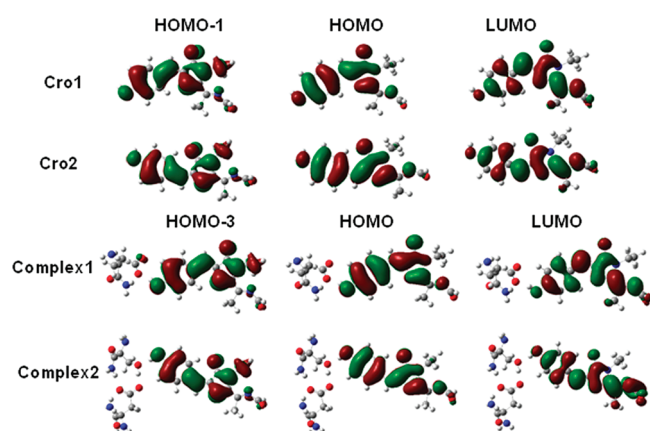
Figure 2. Isosurfaces of the frontier orbitals which participate in the relevant excitations for the studied conformers.
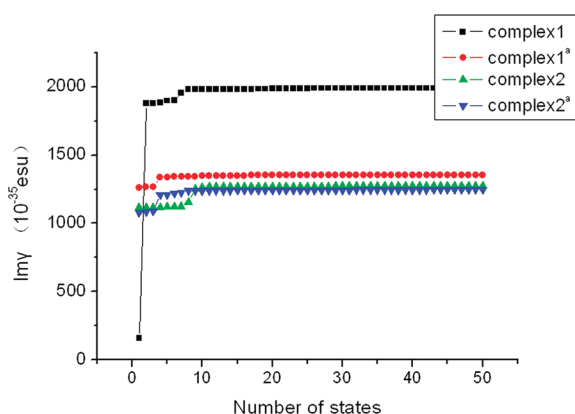
Figure 3. Relationship of the imaginary part of the third-order optical susceptibility and the number of states. The superscript a denotes using the polarizable continuum model (PCM).

Figure 4. Two-photon absorption spectra of complex1 and complex2. The superscript a denotes using the PCM.

Table 6. Two-Photon Absorption Properties of H-Bonding Complexes Obtained at the TDDFT/B3LYP/6-311++G Level: Two-Photon Absorption Wavelength λ_2 (nm), Oscillator Strength f, Two-Photon Absorption Cross Section δ (GM), and Relevant Excitations**

	λ_2 (nm)	transition nature	f	δGM
complex1	1020.6	S0→S2 (H→L) 35%	0.810	34.06
	724.7	S0→S7 (H-5→L) 36%	0.002	38.13
complex1[a]	909.1	S0→S1 (H→L) 39%	0.937	41.18
	685.1	S0→S4 (H-3→L) 38%	0.023	38.90
complex2	926.1	S0→S1 (H→L) 36%	1.038	25.33
	694.7	S0→S9 (H-8→L) 25%	0.030	69.02
complex2[a]	926.1	S0→S1 (H→L) 39%	1.098	26.61
	675.7	S0→S4 (H-3→L) 32%	0.150	73.22

[a] Using PCM at the B3LYP/6-311++G** level.

section, accordingly, we using the TDDFT and SOS methods to calculate the TPA cross section of the H-bonding complex conformers. In the calculation, 50 states were chosen. To ascertain whether 50 states are enough for the convergence of third-order optical polarizability, we investigated the relationship between the imaginary part of the third-order polarizability and the number of states for all of the conformers studied. Figure 3 shows the relationship of the imaginary part of the third-order polarizability and the number of states for the H-bonding complex. The results show that all of the third-order polarizabilities were converged before 50 states.

H-Bonding Complexes. The TPA properties of H-bonding complexes of mKate1 and mKate2 are presented in Figure 4, and

the selected TPA parameters of these H-bonding complexes are listed in Table 6. We find that both the H-bonding complexes of mKate1 and mKate2 have strong TPA bands at about twice wavelength of their first OPA bands. For example, complex1 has the strong TPA band at 909 nm (OPA at 458 nm) with a TPA cross section of 41.18 GM in the PCM model, and complex2 has the strong TPA band at 926 nm (OPA at 460 nm) with a TPA cross section of 26.61 GM in PCM model. These TPA properties agree with the experimental ones.[9] From Figure 4, the TPA band of complex1 including the PCM calculations results in the blue shift with a slight increase in the TPA cross section. Both of the first excited states of complex1 and complex2 are mainly contribution from HOMO−LUMO with $\pi−\pi^*$ character and correspond

10754

dx.doi.org/10.1021/jp203977m |*J. Phys. Chem. B* 2011, 115, 10750–10757

Table 7. NBO Analysis (Using PCM at the B3LYP/6-311++G** Level) of Studied Conformers: The Nature of Donor Orbitals, Acceptor Orbitals, and the Second-Order Perturbation Energies ΔE_2 in kcal/mol

conformer	donor orbital → acceptor orbital	ΔE_2 (kcal/mol)
cro1	LP2 (O14)→LP*1(C1)	59.1
complex1	LP1/LP2 (O16)→BD*1(O14−H 15)	7.71/39.42
	LP2(O14)→LP*1(C1)	71.50
cro2	LP2 (O14)→LP*1(C1)	58.9
complex2	LP1/LP2(O16)→BD*1(O14−H15)	31.51/56.05
	LP1/LP2/LP3(O18)→BD*1(H17−O16)	23.69/4.71/0.11
	LP2 (O14)→LP*1(C1)	63.04

Figure 5. Isosurfaces of intermolecular hyperconjugation of complex1 and complex2.

to the charge transfer states, respectively. Each of these complexes has large differences of the dipole moments between the first excited-state and the ground-state (dipole and transition moments; see the Supporting Information). Furthermore, considering the small transition energy of the first excitations of these H-bonding complexes as mentioned on the former section, these important factors finally result in the strong TPA of the first excited states of these H-bonding complexes according to the dipole term of eq 6.

Except for the strong TPA of the first excited states, the complexes of mKate1 and mKate2 also have strong TPA bands at the shorter wavelength region which correspond to their high excited states. For mKate1, the complex1 shows a strong TPA band at 725 nm with a TPA cross section of 38.13 GM, and this band is blue-shifted to 685 nm with a TPA cross section of 38.90 GM including PCM calculations. For mKate2, complex2 shows a strong TPA band at 695 nm with a TPA cross section of 69.02 GM, and this band is blue-shifted to 676 nm with a TPA cross section of 73.22 GM in the PCM model. We find the TPA cross sections of both complex1 and complex2 including PCM calculations at the wavelength region about 700 nm are closer to the experimental ones.[9] These TPA bands of mKate1 and mKate2 can be attributed to their fourth excitations with contributions from HOMO-3 to LUMO, respectively. From Figure 2, HOMO-3 to LUMO excitations of both mKate1 and mKate2 have $\pi-\pi^*$ character on the phenol ring which corresponds to charge transfer states. These charge transfer states can couple to their first excited state with a large transition dipole moment term of $M_{01}M_{14}$ (dipole and transition moments; see the Supporting Information). These results lead to the strong TPA band at the short wavelength region.

3.4. Charge Transfer and Intermolecular Hyperconjugations. The forming of the H-bonding complex can induce redistribution of electron density in monomers, repolarization of chemical bonds, and rehybridization of atomic orbitals. These changes in electronic structures in monomers lead to changes in molecular structures; furthermore, they result in changes in OPA and TPA properties. Natural bond orbital (NBO) analysis to study orbital interactions within any pair of interacting atoms has become one of the strongest tools available to date to evaluate intermolecular interactions such as hydrogen bonds. NBO analysis was performed using the NBO3.0 program for the conformers which are optimized in the aqueous phase, because in our calculation, these conformers reflect better one- and two-photon absorption properties compared to experimental ones.[9]

The results of NBO analysis are presented in Table 7. In the H-bonding complex, the charge transfer process exists at the
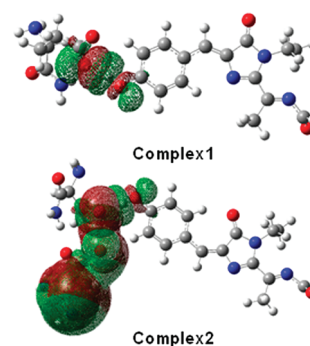
overlap between two molecular orbitals from two monomers. For complex1, the lone pair orbital oxygen (O16) of glutamic acid residues has an overlap with the antibonding orbital σ^*(O14H15) of the chromophore. This intermolecular hyperconjugation (see Figure 5) with the second perturbation stability energy of 39.42 kcal/mol induces a charge transfer from the lone pair of O16 to σ^*(O14H15), which makes the occupation on O16 decrease and the occupation on σ^* (O14H15) increase. The occupation on σ^*(O14H15) of the isolated chromophore is 0.007 e, increasing to 0.101 e when forming the H-bonding complex1. For complex2, there are two intermolecular hyperconjugations which correspond to the two H-bonds in complex2, respectively. The lone pair orbital oxygen (O16) of serine acid residue has an overlap with the antibonding orbital σ^*(O14H15) of chromophore, and the lone pair orbital O18 of aspartic acid residue has an overlap with the antibonding orbital σ^*(O16H17) of the serine acid residue. The intermolecular hyperconjugations of complex2 are presented in Figure 5. Both of these two intermolecular hyperconjugations have large second perturbation stability energy. So these induce a large charge transfer from the lone pair O16 to σ^*(O14H15) and large charge transfer from the lone pair O18 to σ^*(O16H17), respectively. Combined with the two charge transfer process above, we deduce the charge transfers from lone pairs of oxygen (O18 and O16) to the chromophore through these two intermolecular hyperconjugations. Accordingly, intermolecular hyperconjugations of the H-bond form increase the intermolecular charge transfers and second perturbation stability energies of both two complexes. A large TPA cross section of complex2 at about 700 nm originates from a large second perturbation stability energy relative with that of complex1.

Figures 6 and 7 depict the hyperconjugation stabilization interaction between the O16 lone pair and the σ^*(O14H15) orbital in complex1 and complex2. They are sharply diminished with the elongation of the O16···H15, which justifies the presence of the O16···H15−O14 H-bond in complex1 or complex2. The charge transfer interaction within complex1 and complex2 would affect their electronic structure of chromophores. The lone pair orbital of LP2(O14) is almost completely composed of the p-orbital of atom O14, and LP*(C1) is a half-filled orbital which is completely composed of p-orbitals of atom C1, so the intramolecular hyperconjugation LP2(O14)→LP*-(C1) reflects the $p-\pi$ conjugation of phenol ring in the chromophore. From Table 7, the second perturbation stability energy of this intramolecular hyperconjugation is 59.1 kcal/mol in isolate chomophore1 and increases to 71.5 kcal/mol when
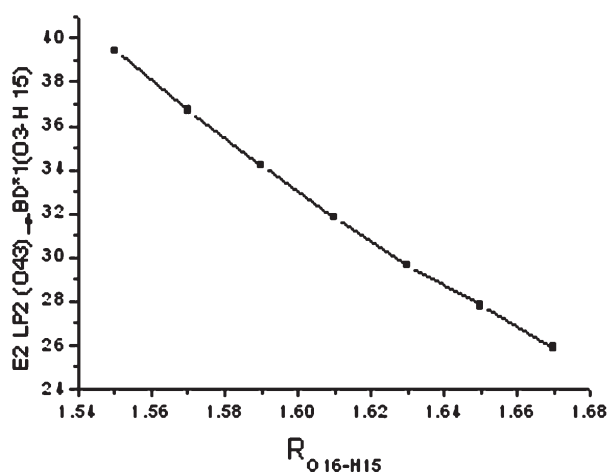
Figure 6. Hyperconjugative interaction energy as a function of the O16—H15 distance of complex1 as obtained from NBO analysis; energy units in kcal/mol.
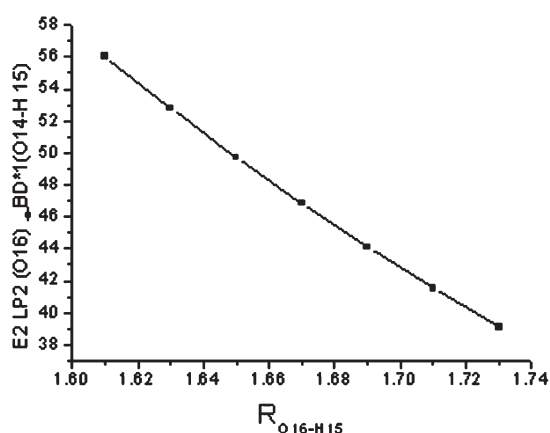

Figure 7. Hyperconjugative interaction energy as a function of O16—H15 distance of complex2 as obtained from NBO analysis; energy units in kcal/mol.

forming the H-bonding complex1. The second perturbation stability energy of intermolecular hyperconjugation LP2(O14)→LP*-(C1) in mKate2 is also increased from isolated chromophore to the H-bonding complex. Combined with the increasing occupation on σ^*(O14H15) due to the intermolecular hyperconjugation, these indicate that there is much more charge transfer from LP2(O14) to LP*(C1) and participate in the $p-\pi$ conjugation of the phenol ring when forming the H-bonding complex; further, enhancement of the $p-\pi$ conjugation would also enhance the π-conjugation interaction of chromophore.

From the above analysis, the intermolecular hyperconjugation of H-bond would be an important influence to the charge transfer state with $\pi-\pi^*$ character, and it directly influences the OPA and TPA spectral properties of the complex. The red-shift OPA band of H-bonding complex corresponds to the electronic transition from HOMO to LUMO with $\pi-\pi^*$ character, and the inter-molecular hyperconjugation of H-bond form increase sthe intermolecular charge transfer from HOMO to LUMO, which leads to the small energy gaps between HOMO and LUMO in complexes. So the complex has a longer wavelength OPA band than that of the isolated chromophore. For TPA properties, the

first strong TPA band of each complex also corresponds to the contribution from the excited state constructed from HOMO to LUMO excitation, so the intermolecular hyperconjugation of the H-bond form contributes to this strong TPA through the increase in intermolecular charge transfer. The second strong TPA of complex at the shorter wavelength region can be attributed to the fourth excitation. The fourth excitation mainly contains HOMO-3 to LUMO contribution with $\pi-\pi^*$character on the phenol ring. So the intermolecular hyperconjugation of H-bond form could increase the intermolecular charge transfer of this state and finally contribute to the strong TPA band of this charge transfer state.

4. CONCLUSION

At first, we have optimized the model structures of isolate chromophores and H-bonding complexes in mKate1 and mKate2 by the DFT/B3lyp/6-311++G(d,p) level in gaseous phase and in aqueous phases. Then we have used the TDDFT method with 6-311++G** basis sets to calculate the OPA and TPA characters of H-bonding complexes of mKate1 and mKate2. Our calculation shows that the H-bonding complex including the PCM calcula-tion (i.e in aqueous) could better reflect the one- and two-photon absorption properties. When forming the H-bonding complex between chromophore and amino acid residue, the intermole-cular hyperconjugation of H-bond form can increase the inter-molecular charge transfer within the complex, enhancing the π-conjugation interaction of the chromophore. These effects are especially influenced on the charge transfer states with $\pi-\pi^*$ character and result in the red-shift OPA band of the H-bonding complex. The calculated hyperconjugate interactions of the hydrogen-bond form show that the strong TPA bands of H-bonding complexes can be attributed to the charge transfer processes within the H-bond of O···H—O.

■ ASSOCIATED CONTENT

ⓢ Supporting Information. Dipole and transition moments at ground and excitation states for studied conformers are listed in tables. This material is available free of charge via the Internet at http://pubs.acs.org.

■ AUTHOR INFORMATION

Corresponding Author
*E-mail: cwd@fjirsm.ac.cn.

■ ACKNOWLEDGMENT

■ REFERENCES

(1) Tsien, R. Y. *Ann. Rev. Biochem* **1998**, *67*, 509–544.
(2) Zipfel, W. R.; Williams, R. M.; Webb, W. W. *Nat. Biotechnol.* **2003**, *21*, 1369–1377.
(3) Shcherbo, D.; Merzlyak, E. M.; Chepurnykh, T. V.; Fradkov, A. F.; Ermakova, G. V.; Solovieva, E. A.; Lukyanov, K. A.; Bogdanova, E. A.; Zaraisky, A. G.; Lukyanov, S.; Chudakov, D. M. *Nat. Methods* **2007**, *4*, 741–746.
(4) Konig, K. *J. Microsc.* **2000**, *200*, 83–104.

(5) So, P. T.; Dong, Y. C.; Masters, B. R. *Annu. Rev. Biomed. Eng.* **2000**, *02*, 399–429.

(6) Lakowicz, J; R, Gryczynski, I; Malak, H.; Schrader, M.; Engelhardt, P.; Kano, H.; Hell, S. W. *Biophys. J.* **1997**, *72*, 567–578.

(7) Squirrell, J. M.; Wokosin, D. L.; White, J. G.; Bavister, B. D. *Nat. Biotechnol.* **1999**, *17*, 763–767.

(8) Drobizhev, M.; Tillo, S.; Makarov, N. S.; Hughes, T. E.; Rebane, A. *J. Phys. Chem. B* **2009**, *113*, 855–859.

(9) Piatkevich, K. D.; Hulit, J.; Subach, O. M.; Wu, B.; Abdulla, A.; Segall, J. E.; Verkhusha, V. V. *Proc. Natl. Acad. Sci. U.S.A.* **2010**, *107*, 5369–5374.

(10) Piatkevich, K.D.; Malashkevich, V. N.; Almo, S. C.; Verkhusha, V. V. *J. Am. Chem. Soc.* **2010**, *132*, 10762–10770.

(11) Lossau, H.; Kummer, A.; Heinecke, R.; PollingerDammer, F.; Kompa, C.; Bieser, G.; Jonsson, T.; Silva, C. M.; Yang, M. M.; Youvan, D. C.; Michel- Beyerle, M. E. *Chem. Phys.* **1996**, *213*, 1–16.

(12) Chattoraj, M.; King, B. A.; Bublitz, G. U.; Boxer, S. G. *Proc. Natl. Acad. Sci. U.S.A.* **1996**, *93*, 8362–8367.

(13) Brejc, K.; Sixma, T. K.; Kitts, P. A.; Kain, S. R.; Tsien, R. Y.; Ormo, M.; Remington, S. J. *Proc. Natl. Acad. Sci. U.S.A.* **1997**, *94*, 2306–2311.

(14) Stoner-Ma, D.; Jaye, A. A.; Matousek, P.; Towrie, M.; Meech, S. R.; Tonge, P. J. *J. Am. Chem. Soc.* **2005**, *127*, 2864–2865.

(15) Grabowski, S. J. *J. Phys. Org. Chem.* **2003**, *16*, 797–802.

(16) Li, A.-Y.; Ji, H.-B.; Cao, L.-J. *J. Chem. Phys.* **2009**, *131*, 164305.

(17) Nifos, R.; Luo, Y. *J. Phys. Chem. B* **2007**, *111*, 14043–14050.

(18) Nifos, R.; Luo, Y. *J. Phys. Chem. B* **2007**, *111*, 505–507.

(19) Olsen, S.; Smith, S. C. *J. Am. Chem. Soc.* **2007**, *129*, 2054–2065.

(20) Koseki, J.; Kita, Y.; Tachikawa, M. *Biophys. Chem.* **2010**, *147*, 140–145.

(21) Frisch, M. J.; Trucks, G. W.; Schlegel, H. B.; et al. *Gaussian 03*; Gaussian, Inc.: Pittsburgh, PA, 2003.

(22) Shchavlev, A. E.; Pankratov, A. N.; Shalabay, A. V. *J. Phys. Chem. A* **2005**, *109*, 4137–4148.

(23) Cossi, M.; Barone, V.; Mennucci, B.; Tomasi, J. *Chem. Phys. Lett.* **1998**, *286*, 253–260.

(24) Mennucci, B.; Tomasi, J. *J. Chem. Phys.* **1997**, *106*, 5151–5158.

(25) Boys, S. F.; Bernadi, F. *Mol. Phys.* **1970**, *19*, 553–566.

(26) Dick, B.; Hochstrasser, R. M.; Trommsdorff, H. P. *Nonlinear Optical Properties of Organic Molecules and Crystals*; Chemla, D. S., Zyss, J., Eds.; Academic Press: Orlando, FL, 1987; Vol. 2, pp 167−170.

(27) Orr, B. J.; Ward, J. F. *Mol. Phys.* **1971**, *20*, 513–526.

(28) Cheng, W.-D.; Wu, D.-S.; Li, X.-D.; Lan, Y.-Z.; Zhang, H.; Chen, D.-G.; Gong, Y.-J.; Zhang, Y.-C.; Li, F.-F.; Shen, J.; Kan, Z.-G. *Phys. Rev. B* **2004**, *70*, 155401–6.

(29) Champagne, B.; Kirtman, B. *J. Chem. Phys.* **2006**, *125*, 024101–7.

(30) Beljonne, D.; Wenseleers, W.; Zojer, E.; Shuai, Z.; Vogel, H.; Pond, S. J. K.; Perry, J. W.; Marder, S. R.; Jean-Luc, B. *Adv. Funct. Matter* **2002**, *12*, 631–641.

(31) Terenziani, F.; Katan, C.; Badaeva, E.; Tretiak, S.; Blanchard-Desce, M. *Adv. Mater.* **2008**, *20*, 4641–4678.

(32) Ohta, K.; Antonov, L.; Yamada, S.; Kamada, K. *J. Chem. Phys.* **2007**, *127*, 084504–12.

(33) Pierce, B. M. *J. Chem. Phys.* **1989**, *91*, 791–811.

(34) Gisbergen, S. J. A.; van.; Snijders, J. G.; Baerends, E. J. *Comput. Phys. Commun.* **1999**, *118*, 119–138.

(35) Li, X.-D.; Cheng, W.-D.; Wu, D.-S.; Lan, Y.-Z.; Zhang, H.; Gong, Y.-J.; Li, F.-F.; Shen, J. *J. Phys. Chem. B* **2005**, *109*, 5574–5579.

(36) Cheng, W.-D.; Wu, D.-S.; Zhang, H.; Chen, J.-T. *J. Phys. Chem. B* **2001**, *105*, 11221–11226.

(37) Maroulis, G.; Karamanis, P.; Pouchan, C. *J. Chem. Phys.* **2007**, *126*, 154316–5.

10757

dx.doi.org/10.1021/jp203977m |*J. Phys. Chem. B* 2011, 115, 10750–10757